HHS Public Access

Author manuscript

*Med Phys*. Author manuscript; available in PMC 2024 January 01.

Published in final edited form as:

*Med Phys*. 2023 January ; 50(1): 440–448. doi:10.1002/mp.16047.

# Auto-detection of necessity for MRI-guided online adaptive replanning using a machine learning classifier

**Abdul K. Parchur**,

**Sara Lim**,

**Haidy Nasief**,

**Eenas Omari**,

**Ying Zhang**,

**Eric Paulson**,

**William Hall**,

**Beth Erickson**,

**X. Allen Li***

Department of Radiation Oncology, Medical College of Wisconsin, Milwaukee, 53226 USA

## Abstract

**Purpose:** MRI-guided adaptive radiation therapy (MRgART), particularly daily online adaptive replanning (OLAR) can substantially improve radiation therapy delivery, however it can be labor-intensive and time-consuming. Currently, the decision to perform OLAR for a treatment fraction is determined subjectively. In this work, we develop a machine learning algorithm based on structural similarity index measure (SSIM) and change in entropy to quickly and objectively determine whether OLAR is necessary for a daily MRI set.

**Methods:** A total of 109 daily MRI sets acquired on a 1.5T MR-Linac during MRgART for 22 pancreatic cancer patients each treated with five fractions were retrospectively analyzed. For each daily MRI set, OLAR and reposition (No-OLAR) plans were created and the superior plan with the daily fraction determined per clinical dose-volume criteria. SSIM and entropy maps were extracted from each daily MRI set, with respective to its reference (e.g., dry-run) MRI in the region enclosed by 50–100% isodose surfaces. A total of six common features were extracted from SSIM maps. Pearson's rank correlation coefficient was utilized to rule-out redundant SSIM features. A t-test was used to determine significant SSIM features which were combined with the change in entropy to develop ensemble machine classifier with 5-fold cross validation. The performance of the classifier was evaluated using the area under curve (AUC) of the receiver operating characteristic (ROC) curve.

**Results:** A machine learning classifier model using two SSIM features (mean and full width at half maximum) and change in entropy was determined to be able to significantly discriminate between No-OLAR and OLAR groups. The obtained machine learning ensemble classifier can predict OLAR necessity with a cross validated AUC of 0.93. Misclassification

*Author to whom correspondence should be addressed. Ali@mcw.edu, Telephone: +1 (414) 805 4362.

was found primarily for No-OLAR cases with dosimetric plan quality closely comparable to the corresponding OLAR plans, thus, are not a major practical concern.

**Conclusion:** A machine learning classifier based on simple first-order image features, i.e., SSIM features and change in entropy, was developed to determine when OLAR is necessary for a daily MRI set with practical acceptable prediction accuracy. This classifier may be implemented in the MRgART process to automatically and objectively determine if OLAR is required following daily MRI.

### Keywords

MR-guided radiation therapy; structural similarity index measure; adaptive radiation therapy; online adaptive replanning; pancreatic cancer

## 1. INTRODUCTION

During radiation therapy (RT) delivery, the location, shape, and size of tumors and organs at risk (OARs) can change significantly between treatment fractions primarily due to unreproducible patient setup errors and patient-specific changes in anatomy, physiology, and treatment response[1,2]. These inter-fraction changes can hinder the effectiveness of RT. The current standard of care to address the inter-fraction variations is to use image-guided RT (IGRT) to reposition the patient based on the daily image while delivering the same treatment plan (i.e., reference plan) for all fractions. However, IGRT repositioning primarily addresses translational errors, therefore it cannot fully account for all inter-fraction changes. To improve IGRT, adaptive RT (ART) is being developed[3,4]. In particular, online adaptive re-planning (OLAR) requires accurate delineation of OARs and targets based on the daily anatomy and the creation of an adaptive plan for the treatment fraction, which has the potential to fully address inter-fractional variations[5].

With the recent commercial introduction of hybrid MRI scanner and linear accelerator systems (MR-Linac), MRI-guided adaptive radiation therapy (MRgART), particularly MR-guided OLAR, is being rapidly implemented and practiced in the clinic[6–8]. Compared to common image modalities for IGRT, e.g., CT, cone-beam CT, MRI provides superior soft-tissue contrast, functional information of tumor and OARs, and real-time imaging during RT delivery. Recently, Paulson *et al.*,[9] reported the clinical use of a MR-Linac system which integrates 1.5 Tesla MRI and 7 MV Linac (Unity, Elekta AB). The Unity MR-Linac system offers two adaptive planning techniques to address the inter-fraction variations based on daily MRI: (i) Adapt-to-position (ATP, i.e., No-OLAR), in which the reference plan is reoptimized with an isocenter shift determined from the co-registration of the daily MRI and the reference image, and ii) Adapt-to-shape (ATS, i.e., OLAR), in which a new plan is generated based on the anatomy of the day from the daily MRI[9]. The Unity system offers six different algorithms to optimize OLAR plans: (1) original segments, (2) adapt segments, (3) optimize weights from segments, (4) optimize weights from fluence, (5) optimize weights and shapes from segments, and (6) optimize weights and shapes from fluence[10]. Another MR-Linac system, MRIdian, (ViewRay Inc) uses similar workflow (called “on-table adaptation”) for OLAR and a reposition workflow (adjusting table) for No-OLAR[11]. While the No-OLAR workflow in both systems is similar to IGRT

repositioning, primarily accounting for translational shifts, the OLAR workflow can fully correct for inter-fraction variations.

With today's technology, OLAR is a complex, labor-intensive, and time-consuming process requiring delineation based on the anatomy of the day, plan optimization, evaluation, and quality assurance (QA) using the newly acquired daily image. It has been well documented by several early adopters of MRgART that the OLAR can take up to 90 min[12]. Paulson *et al.*,[9] reported a median time of 62 min for using OLAR to treat abdominal tumors. The times required for OLAR with the ViewRay MRgART system were in the range of 30–80 minutes according to the study by Görkem *et al*[12]. Along with the prolonged time, OLAR requires substantial radiation oncology staffing for real-time input and decision making at the treatment console.

On the other hand, OLAR is not necessary for all treatment fractions. For a fraction with minimal interfractional deformation, IGRT repositioning (No-OLAR) may be sufficient. Based on the study by Omari *et a*l,[13] approximately 2/3 of the treatment fractions for pancreatic cancer require OLAR. Thus, in clinical practice, it is desirable to determine when OLAR is necessary before substantial effort (e.g., re-contouring on daily image) is spent[14,15]. Our previous study on this topic based on CTs,[14] showed that the Jacobian determinant histogram (JDH) obtained from deformable image registration (DIR) between reference (planning) and daily CTs can be used to determine the necessity of OLAR for prostate where deformation is largely limited to expansion/contraction of the rectum and bladder.

Although this JDH method works reasonably for CT in a tumor site with not too complex deformation, it is not suitable for MRI in the abdomen primarily due to inaccurate DIR for the complexity and the lack of trends for the organ deformation in abdomen. Consequently, parameters derived from the DIR (e.g., JDH, deformation vector field) may not be able to accurately measure the actual organ deformation. Currently, the decision to perform OLAR for a treatment fraction during MRgART is determined either empirically (e.g., based on fractionation) or by subjectively inspecting the daily MRI after it is acquired[16]. This practice cannot ensure OLAR is used only when it is necessary.

Structural similarity index measure (SSIM) is introduced to quantitatively assess the similarity between two images[17,18]. The purpose of this study is to investigate whether the first-order features from SSIM and change in entropy calculated between reference and a daily MRI can be used to robustly determine the necessity of OLAR for a daily fraction based on the differences (e.g., organ deformation) between the two MRI sets. SSIM and entropy maps can be calculated immediately following the acquisition of the daily MRI without the need of labor-intensive and time-consuming segmentation.

## 2. MATERIALS AND METHODS

### 2.1 MRI Data

In this IRB approved HIPAA compliant study, a total of 109 daily MRI sets and 22 dry-run MRI sets acquired during MRgART for 22 pancreatic cancer patients were retrospectively

analyzed. These patients were treated with SBRT in five fractions using either the No-OLAR or OLAR workflow on an MRI-Linac (Unity, Elekta) from January 2019 to June 2021. In our practice, we schedule a zero fraction for each patient to acquire "dry-run MRI" on the Unity without treatment, ensuring the quality of daily MRI is appropriate for the patient. Both the dry-run and daily MRIs were acquired under free breathing using an in-house developed 4D-MRI technique[9,19]. A dose of 3300 cGy in 5 fractions was used for the treatment. The motion-averaged images derived from the 4D-MRI were used for the daily planning image. A high-performance computer server located in the MR-Linac machine network was used for the rapid reconstruction and processing of 4D-MRI. All dry-run and daily MRI datasets were preprocessed using a standardization process including bias correction and Gaussian smoothing, as depicted in FIG 1. The bias correction was applied to correct for the RF coil inhomogeneity via an intensity-based nonparametric bias correction method, i.e., N4 algorithm, followed by Gaussian smoothing used to smooth noisy pixels while preserving the intensity of most edges[20]. The obtained dry-run and daily MRIs were rigidly registered and the contours on the dry-run MRI were transferred onto the daily MRI using a software (MIM Software Inc., Version 7.0.6, Cleveland, OH).

### 2.2 Plan Generation

For each patient, a reference plan was created based on the dry-run MRI. For each daily MRI set, a pair of plans, i.e., No-OLAR and OLAR plans, were generated using a treatment planning system (MonacoTM V5.4, Elekta, Stockholm, Sweden). The dose calculation was performed with a graphics processing unit (GPU) accelerated Monte Carlo dose (GPUMCD) engine considering a transverse 1.5 T magnetic field using a calculation grid size of 3 mm and statistical uncertainty of 1% per calculation[9,21,22]. For each daily MRI set, the qualities of the plan pair were compared based on the dose distribution and commonly used dose-volume criteria of the target (e.g., planning target volume, PTV) and OARs used in our clinic as shown in Table 1. Currently, these constraints are being used for a clinical trial (ClinicalTrials.gov Identifier: NCT03704662) in treating locally advanced type-A pancreatic adenocarcinoma patients[23]. For example, a plan with satisfied target coverage and better OAR sparing was considered superior. For two plans with similar OAR sparing, the plan with higher target coverage was considered superior. Two plans with similar target coverage and OAR sparing were considered as comparable. The plan quality was assessed by an experienced physicist and was independently verified by two other investigators to minimize the subjectiveness. All daily MRI sets were divided into OLAR and No-OLAR groups. A daily MRI set with its OLAR plan superior to its No-OLAR plan was classified as an OLAR set, while a daily MRI set with its No-OLAR plan equivalent or comparable to its OLAR was called No-OLAR set.

### 2.3 Structural Similarity Index Measure and Entropy

For each patient, selected isodose surfaces (IDS) from the reference plans were converted into structures and transferred to each daily MRI set via rigid registration using the MIM software tool. To minimize residual registration errors, local registration using a box-based assisted alignment algorithm was applied by drawing the box enclosing the selected IDSs. SSIM map and entropy map were generated to extract quantitative features from the solid

regions enclosing the 50%, 80%, and 100% IDS and in the shells enclosing 50–80%, 80–100%, and 50–100% IDS.

SSIM values were extracted in these enclosed regions between the reference and each daily MRI set using '*multissim3*' function in MATLAB (R2020b), based on multiplicative combination of the three terms, luminance (l), contrast (c), and structural (s), as shown in the equations below15:

$$SSIM(x,y) = [l(x,y)]^{\alpha} . [c(x,y)]^{\beta} . [s(x,y)]^{\gamma} \quad (1)$$

$$l(x,y) = \frac{2\mu_x\mu_y + C1}{\mu_x^2 + \mu_y^2 + C1} \quad (2)$$

$$c(x,y) = \frac{2\sigma_x\sigma_y + C2}{\sigma_x^2 + \sigma_y^2 + C2} \quad (3)$$

$$s(x,y) = \frac{\sigma_{xy} + C3}{\sigma_x\sigma_y + C3} \quad (4)$$

where $\mu_x$, $\mu_y$, $\sigma_x$,$\sigma_y$, and $\sigma_{xy}$ are the local means, standard deviations, and cross-covariances of x and y, respectively. The indices *l and c* are limited between 0 and 1, and the *s* index is limited between −1 and +1. *C1, C2*, and *C3* are the small constants introduced to evade numerical instability when the denominator approaches zero. It was determined that the appropriate region where the anatomy deformation measured by SSIM was most relevant for OLAR (e.g., with high dose gradience) was the ring (shell in 3D) enclosed by the 50–100% IDS. Unless otherwise specified, all SSIM data reported hereafter were calculated in the 50–100% rings (shells). SSIM value of 1.0 refers to identical reference and daily MRIs in the selected regions. The entire data analysis workflow is depicted in FIG. 2A. FIG. 2B shows a sample of the axial views of the rings enclosed by the 50–100% IDSs on a representative daily MRI set (left), and their corresponding SSIM maps (right) obtained between the daily and reference MRI sets, where higher SSIM values are represented by the bright yellow regions and lower values are represented by the dark regions. FIG. 2C shows an example of the SSIM map (left) and its corresponding histogram (right). Six commonly used features, i.e., mean, median, moment (2nd order), skewness, kurtosis, full width at half maximum (FWHM)[24,25], were extracted from the SSIM maps for all daily MRI sets.

Similarly, the total change in local entropy (Δ entropy) between daily and Ref MRI sets was calculated from the entropy map as shown in Eq. 5, which determines statistical measure of randomness within 50–100% IDSs.

$$\Delta\ Entropy = \frac{1 + Log(Daily\ Entropy) - Log(Ref\ Entropy)}{Log(Daily\ Entropy)} \times 10 \quad (5)$$

Correlations of these features to No-OLAR or OLAR groups were analyzed to identify features with significant difference between No-OLAR and OLAR groups by Pearson's

rank correlation in RStudio (Version 1.1.456) using the 'Performance Analytics' package (Version 2.04) and 'corrplot' package (Version 0.92) in the Anaconda environment. The best performing features were determined by using t-test p-values and Pearson's rank correlation.

### 2.4 Machine Learning Analysis

Multiple classification models were trained using simple decision tree, fine Gaussian SVM, complex trees, Bayesian classifier, and KNN in MATLAB's classification learner app using 2–3 features combination to determine the best performing model. A 5-fold cross validation process was used to optimize the model hyperparameter. To construct a deeper tree an ensemble bagged tree classifier was also used, it starts by bagging a weak learner as a KNN, discriminant or decision tree on the data set and generate bootstrap replicas of the data set to grow the decision trees on the replicas. For this study, the weak learner was set to be a decision tree with the number of learners for the ensemble bagged tree classifier set to 100 with 0.1 shrinkage learning rate. Model performance, i.e., predicting whether No-OLAR or OLAR should be used for a daily MRI, was judged using the area under the receiver operator characteristic plot (AUC of the ROC curve). The entire process for developing the structural similarity and change in entropy-based OLAR and No-OLAR prediction model is shown in FIG. 2A. Misclassification (inaccuracy) of the obtained model was analyzed.

## 3. RESULTS

Spearman correlations showed that three SSIM features and change in entropy were not redundant. These features passed the t-test ($p<0.005$) indicating significant differences between the No-OLAR and OLAR groups. FIG. 3 shows the analysis of the six SSIM features and Δ entropy, showing (A) the Pearson correlation matrix of the seven features with No-OLAR and OLAR group, i.e., distribution of each variable along the diagonal with bivariate scatter plots, the significance levels and its Pearson's correlation rank, (B) the Pearson rank of the non-redundant features with $p<0.005$. FIG 4A represents the boxplot visualization of the (i) mean, (ii) FWHM, and (iii) Δ entropy, the p-values obtained using t-test analysis between OLAR and No-OLAR group is represented in the inset of the figure itself. The box plot in FIG 4A shows separation of the means between No-OLAR and OLAR groups with ◇ shaped symbol. Based on the analysis, the best performing three features that can be used to separate the No-OLAR and OLAR groups was determined to be mean, FWHM, and Δ entropy.

The best performing model was an ensemble classifier with three features combination (SSIM mean, SSIM FWHM, Δ entropy) with an AUC of 0.93. FIG 4B and 4C represents the ensemble classifier analysis results using three features, which predicts the OLAR necessity with 5-fold cross validation. FIG. 4B and 4C depict the confusion matrices and receiver operating characteristic (ROC) curves, respectively, for the obtained results using ensemble classifier to predict the No-OLAR and the OLAR cases with AUC of 0.93.

The obtained model misclassified four fractions in the testing dataset. FIG 5 presents the dosimetric comparisons between the OLAR and NO-OLAR plans for all the four misclassification fractions (4 cases). It is seen that the difference in the plan qualities between the OLAR and No-OLAR plans for these cases can be considered marginal. For

example, for case 1, the PTV coverage (V3300cGy) of > 95% was satisfied by both the No-OLAR (95.01%) and OLAR (96.3%) plans, while the stomach constraints of V2650cGy < 5cc and V2000cGy < 20cc were slightly violated in the No-OLAR plan.

## 4. DISCUSSION

It is desirable to quickly and objectively determine when OLAR is needed during adaptive radiation therapy since OLAR can be labor-intensive and time-consuming and is not necessary for all treatment fractions. In this work, a simple machine learning classifier based on first-order structural similarity texture features such as SSIM and change in entropy was developed to automatically determine whether OLAR is necessary for a given daily MRI set. The development process starts by first identifying the best performing features, which are classified OLAR *vs* No-OLAR with high significance ($p<0.05$). Even though some of the individual features in classifying No-OLAR *vs* OLAR groups were significantly different, still the single feature performance was not high enough.

We found that an ensemble classifier with three features combination increased the model performance and was able to differentiate between the two groups with an AUC of 0.93. The obtained classifier model can be implemented in MRgART workflow immediately following the daily MRI acquisition by: (1) populating the reference plan created offline by rigidly registering the daily and reference MRIs, (2) calculating SSIM and entropy maps in the region enclosing the 50–100% IDSs between the daily and reference MRIs, (3) extracting mean and FWHM from SSIM map, and Δ entropy from entropy map, and (4) applying the obtained three feature values to the classifier model derived in this work to determine whether OLAR should be used for the fraction. This process can be fully automated and can quickly and objectively determine if OLAR is beneficial for the treatment fraction prior to initiating the time-consuming and labor-intensive OLAR workflow.

Since OLAR can account for organ deformation while No-OLAR cannot, it is necessary to identify an appropriate region where the magnitude of structure deformation determines the necessity of using OLAR *vs* No-OLAR. Our analysis indicates that in the region enclosed by 50–100% IDSs, the SSIM-based classification performed best. Subsequently, all data presented in this paper was based on the analysis in this region. The AUC of 0.93 for the developed model is practically acceptable. The close examination of the wrong predication (misclassification) fractions (FIG. 5) revealed that the plan quality between the No-OLAR and OLAR plans for these failure fractions were comparable, implying that a wrong prediction for such a fraction would not result in significant dosimetric consequences. Furthermore, the simple model obtained is efficient in classifying OLAR cases with greater accuracy compared to No-OLAR cases (94% vs, 78%, FIG 4B). The four No-OLAR cases misclassified showed very comparable target coverage (all >~95%) and OAR sparing (~1.23% difference) compared to the corresponding OLAR plans (FIG. 5).

There are some limitations to our study. For PTVs with small volumes (<10 cc), the developed classifier may not be applicable. For such cases, it was observed that the 50–100% IDSs enclosed shells were thin, resulting in a very small number of voxels in the structural similarity texture matrix, which can lead to inaccuracy in extracting features. We

used the dry-run MRI as the reference image to create a reference plan and to register it to daily MRIs to calculate SSIM for each fraction. The dry-run MRI, instead of the recent daily MRI, was used as a reference to avoid additional effort e.g., verifying contours and plan on each daily MRI which will increase the difficulty in clinical implementation. Furthermore, we were using rigid registration instead of DIR for the considerations that (1) the rigid registration would be substantially faster than DIR in the future implementation, and (2) DIR is problematic to address large deformations in abdomen.

Increasing the dataset size in future studies will improve the machine learning classifier performance. Currently, a five-fold cross validation was implemented to estimate the classifier performance due to the limited data size. A more generalizable approach currently being investigated in our group is to add higher order features, such as multiscale wavelet texture features using a sophisticated machine learning algorithm to predict OLAR necessity[26]. Multiscale wavelet texture features can distinguish No-OLAR and OLAR plans with close dosimetric differences, thus increasing the classification accuracy as compared to first-order SSIM and entropy-based features. In general, first-order texture features may not be able to encode invisible patterns from MRI sets as wavelet-based multiscale texture features can. The high model accuracy of OLAR group patients (~94%) makes the model more valuable in the clinic, although extracting more specific higher order features further improves classifier performance. Nonetheless, the simpler SSIM and entropy-based classifier model is more intuitive and can be more easily understood as compared to the complex wavelet features. This classifier is suitable for use as a secondary check of the prediction from the wavelet classifier due to its easy 2D visual projection of misclassification region on axial MR slices. Such a secondary check is generally desirable in a fully automated process. Also, SSIM maps intuitively illustrate differences in daily MR imaging compared to reference MR imaging.

Personnel scheduling has been a major issue in MRgART in some clinics. Being able to quickly and automatically determine if OLAR is needed, while cannot fully resolve the scheduling issue, may help avoid unnecessary personnel effort and save time for the patient and the machine. For example, certain team members of MRgART (radiation oncologist, physicist, and/or dosimetrist) can be relieved for other tasks once the OLAR is determined to be unnecessary. Currently, active research and development efforts for fully automated MRgART process (e.g., auto-contouring, auto-planning) are ongoing. The present work can be a part of the automated process where staff scheduling may no longer be a major issue.

## 5. CONCLUSIONS

A machine learning classifier based on first-order image features (SSIM and change in entropy features) was developed to determine when OLAR is necessary for a daily MRI set with acceptable prediction accuracy. First-order texture-based features can identify underlying residual anatomical changes of the daily MRI data set, which results in an AUC of 93% in predicting OLAR necessity. The process of using the ensemble classifier model can be fully automated and incorporated into the MRgART workflow to quickly and objectively determine if OLAR is needed immediately following the daily MRI acquisition.

Further studies with larger datasets are needed to validate the process and to improve the performance of the classifier.

## ACKNOWLEDGEMENTS

The authors would like to thank Dr. Jiaofeng Xu and Mr. Virgil Willcut from Elekta for their input.

### FUNDING STATEMENT

The research was partially supported by the Medical College of Wisconsin (MCW) Cancer Center and Froedtert Hospital Foundation, the MCW Meinerz and Fotsch Foundations, and the National Cancer Institute of the National Institutes of Health under award number R01CA247960. The content is solely the responsibility of the authors and does not necessarily represent the official views of the National Institutes of Health.

## REFERENCES

1. Yan D, Lockman D, Martinez A, et al. Computed tomography guided management of interfractional patient variation [published online ahead of print 2005/06/29]. Semin Radiat Oncol. 2005;15(3):168–179. [PubMed: 15983942]
2. Li XA, Qi XS, Pitterle M, et al. Interfractional variations in patient setup and anatomic change assessed by daily computed tomography [published online ahead of print 2007/03/03]. Int J Radiat Oncol Biol Phys. 2007;68(2):581–591. [PubMed: 17331669]
3. Yan D, Vicini F, Wong J, Martinez A. Adaptive radiation therapy [published online ahead of print 1997/01/01]. Phys Med Biol. 1997;42(1):123–132. [PubMed: 9015813]
4. Li XA. Adaptive Radiation Therapy [published online ahead of print 2011/07/01]. Med Phys. 2011;38(7):4467–4468.
5. Glide-Hurst CK, Lee P, Yock AD, et al. Adaptive Radiation Therapy (ART) Strategies and Technical Considerations: A State of the ART Review From NRG Oncology [published online ahead of print 20201024]. Int J Radiat Oncol Biol Phys. 2021;109(4):1054–1075. [PubMed: 33470210]
6. Lagendijk JJ, Raaymakers BW, van Vulpen M. The magnetic resonance imaging-linac system [published online ahead of print 2014/06/17]. Semin Radiat Oncol. 2014;24(3):207–209. [PubMed: 24931095]
7. Mutic S, Dempsey JF. The ViewRay system: magnetic resonance-guided and controlled radiotherapy. Semin Radiat Oncol. 2014;24(3):196–199. [PubMed: 24931092]
8. Green OL, Henke LE, Hugo GD. Practical Clinical Workflows for Online and Offline Adaptive Radiation Therapy [published online ahead of print 2019/04/28]. Semin Radiat Oncol. 2019;29(3):219–227. [PubMed: 31027639]
9. Paulson ES, Ahunbay E, Chen X, et al. 4D-MRI driven MR-guided online adaptive radiotherapy for abdominal stereotactic body radiation therapy on a high field MR-Linac: Implementation and initial clinical experience [published online ahead of print 2020/06/04]. Clin Transl Radiat Oncol. 2020;23:72–79. [PubMed: 32490218]
10. Winkel D, Bol GH, Kroon PS, et al. Adaptive radiotherapy: The Elekta Unity MR-linac concept [published online ahead of print 2019/07/26]. Clin Transl Radiat Oncol. 2019;18:54–59. [PubMed: 31341976]
11. van Timmeren JE, Chamberlain M, Krayenbuehl J, et al. Treatment plan quality during online adaptive re-planning [published online ahead of print 2020/08/23]. Radiat Oncol. 2020;15(1):203. [PubMed: 32825848]
12. Görkem G, Serbez I, Temur B, et al. Time Analysis of Online Adaptive Magnetic Resonance-Guided Radiation Therapy Workflow According to Anatomical Sites [published online ahead of print 2020/08/03]. Pract Radiat Oncol. 2021;11(1):e11–e21. [PubMed: 32739438]
13. Omari E, Nasief H, Zhang Y, et al. Should Daily Online Adaptive Replanning be Utilized for Every Treatment in MRI-Guided Radiotherapy for Pancreatic Cancer? [published online ahead of print 2021/10/28]. Int J Radiat Oncol Biol Phys. 2021;111(3S):e66.

14. Lim SN, Ahunbay EE, Nasief H, Zheng C, Lawton C, Li XA. Indications of Online Adaptive Replanning Based On Organ Deformation [published online ahead of print 20190822]. Pract Radiat Oncol. 2020;10(2):e95–e102. [PubMed: 31446149]
15. Brown E, Owen R, Harden F, et al. Predicting the need for adaptive radiotherapy in head and neck cancer. Radiother Oncol. 2015;116(1):57–63. [PubMed: 26142268]
16. Wang Z, Simoncelli EP, Bovik AC. Multiscale structural similarity for image quality assessment. Paper presented at: The Thrity-Seventh Asilomar Conference on Signals, Systems & Computers, 2003; 9–12 Nov. 2003, 2003.
17. Wang Z, Bovik AC, Sheikh HR, Simoncelli EP. Image quality assessment: from error visibility to structural similarity [published online ahead of print 2004/09/21]. IEEE Trans Image Process. 2004;13(4):600–612. [PubMed: 15376593]
18. Renieblas GP, Nogues AT, Gonzalez AM, Gomez-Leon N, Del Castillo EG. Structural similarity index family for image quality assessment in radiological images [published online ahead of print 2017/09/20]. J Med Imaging (Bellingham). 2017;4(3):035501. [PubMed: 28924574]
19. Mickevicius NJ, Paulson ES. On the use of low-dimensional temporal subspace constraints to reduce reconstruction time and improve image quality of accelerated 4D-MRI [published online ahead of print 2021/01/08]. Radiother Oncol. 2021;158:215–223. [PubMed: 33412207]
20. Zhang Y, Paulson E, Lim S, et al. A Patient-Specific Autosegmentation Strategy Using Multi-Input Deformable Image Registration for Magnetic Resonance Imaging–Guided Online Adaptive Radiation Therapy: A Feasibility Study. Advances in Radiation Oncology. 2020;5(6):1350–1358. [PubMed: 33305098]
21. Hissoiny S, Ozell B, Bouchard H, Despres P. GPUMCD: A new GPU-oriented Monte Carlo dose calculation platform. Med Phys. 2011;38(2):754–764. [PubMed: 21452713]
22. Hissoiny S, Raaijmakers AJ, Ozell B, Despres P, Raaymakers BW. Fast dose calculation in magnetic fields with GPUMCD [published online ahead of print 20110720]. Phys Med Biol. 2011;56(16):5119–5129. [PubMed: 21775790]
23. National Library of Medicine (U.S.). (2018, October 10–2030, December 1). Preoperative Fractionated Radiation Therapy Versus Stereotactic Body Radiation Therapy for Resectable or Borderline Resectable, or Locally Advanced Type A Pancreatic Adenocarcinoma. ClinicalTrials.gov Identifier: NCT03704662.
24. Liu X, Maleki F, Muthukrishnan N, et al. Site-Specific Variation in Radiomic Features of Head and Neck Squamous Cell Carcinoma and Its Impact on Machine Learning Models [published online ahead of print 2021/08/08]. Cancers (Basel). 2021;13(15).
25. Nasief H, Zheng C, Schott D, et al. A machine learning based delta-radiomics process for early prediction of treatment response of pancreatic cancer [published online ahead of print 2019/10/12]. NPJ Precis Oncol. 2019;3:25. [PubMed: 31602401]
26. Nasief H, Omari E, Zhang Y, et al. Automatically Determining Necessity of Online Adaptive Replanning Based on MRI Wavelet Multiscale Texture Features for MRI-Guided Adaptive Radiation Therapy. International Journal of Radiation Oncology, Biology, Physics. 2021;111(3):S55.

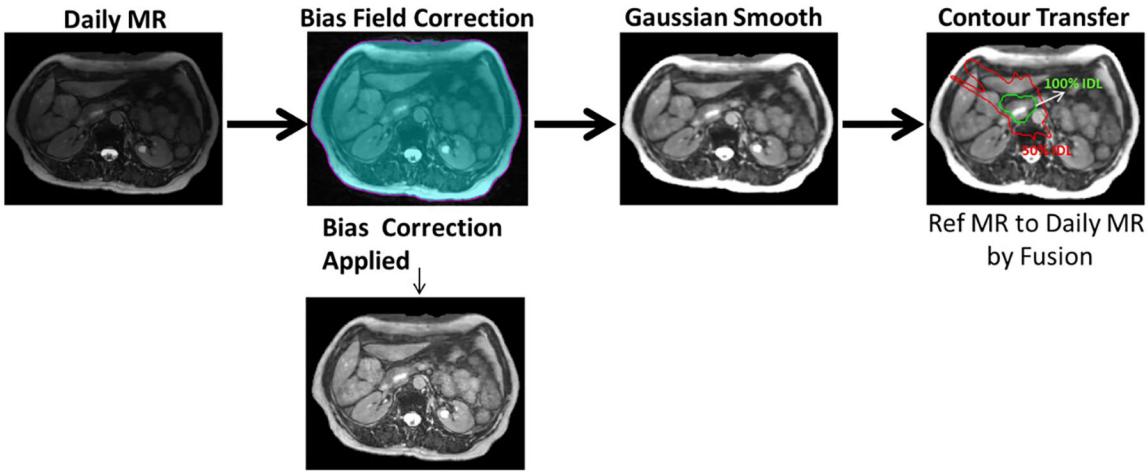


**FIG 1.**

Schematic representation for dry-run and daily MRI standardization, including bias correction, Gaussian smoothing, before their registration and the contour transfer from reference MRI to daily MRI.

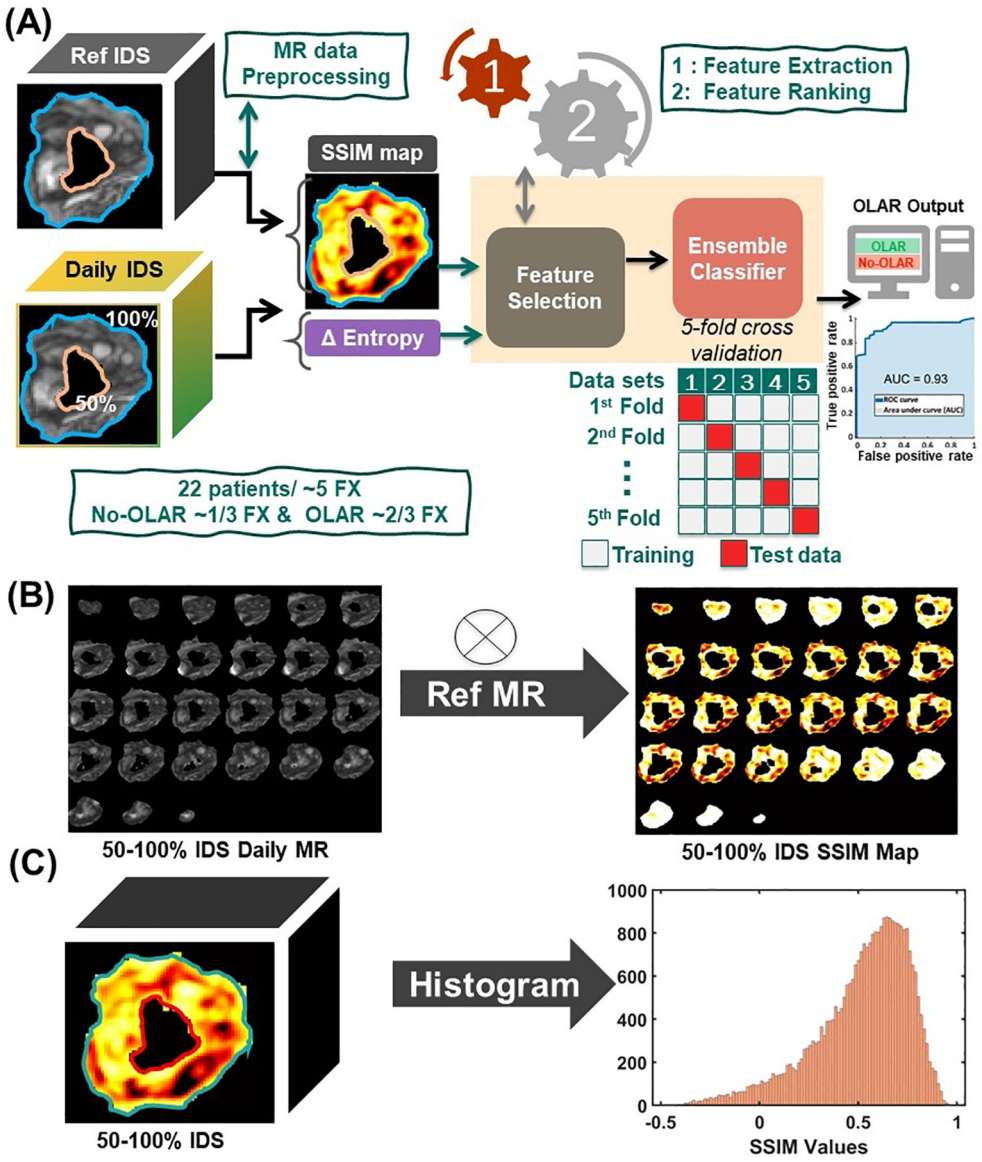


**FIG 2.**

(A) Schematic representation of data analysis workflow from extracting SSIM and change in entropy (Δ entropy) between reference and daily MRIs in the region enclosed by 50–100% iso-dose surfaces (IDSs) to establishing optimizable support vector machine classifier with the 5-fold cross validation. (B) Typical axial views of the rings enclosed by 50 and 100% IDSs of a daily MRI set (left) and the corresponding SSIM maps (right), (C) an example of 3D SSIM map in the region enclosing the 50–100% IDSs (left) and the SSIM histogram (right).

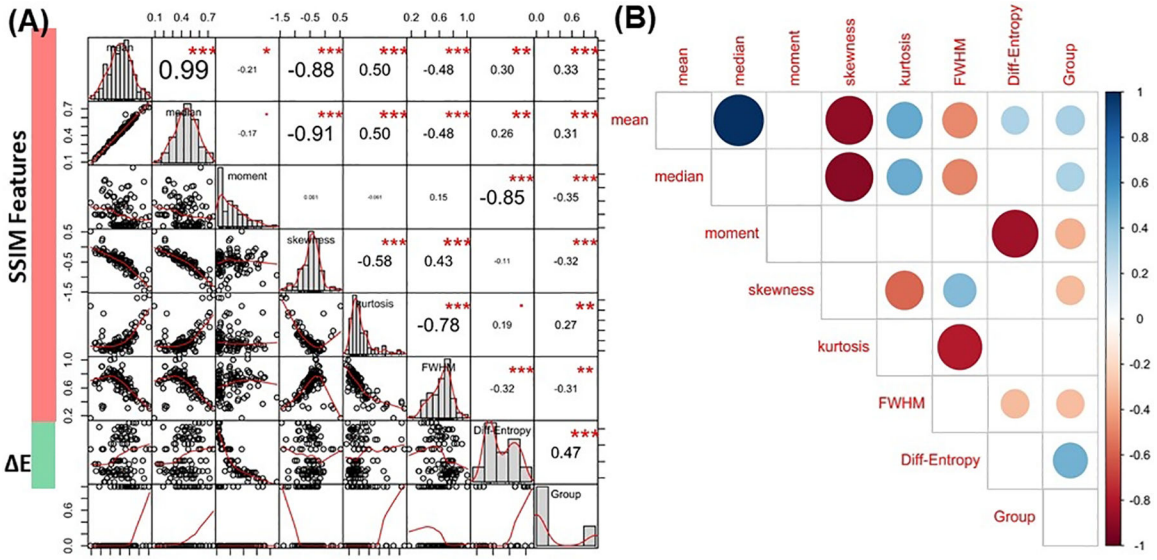


**FIG 3.**

Analyses of SSIM and Δ entropy features, (A) Pearson correlation matrix analysis of SSIM and Δ entropy features with correlation histograms and p-values, (B) Pearson rank of correlation matrix to features with *p*-value <0.005, with Pearson rank indicated by the size and the color of the circles, where red, and blue colors indicate a negative or a positive correlation, respectively.

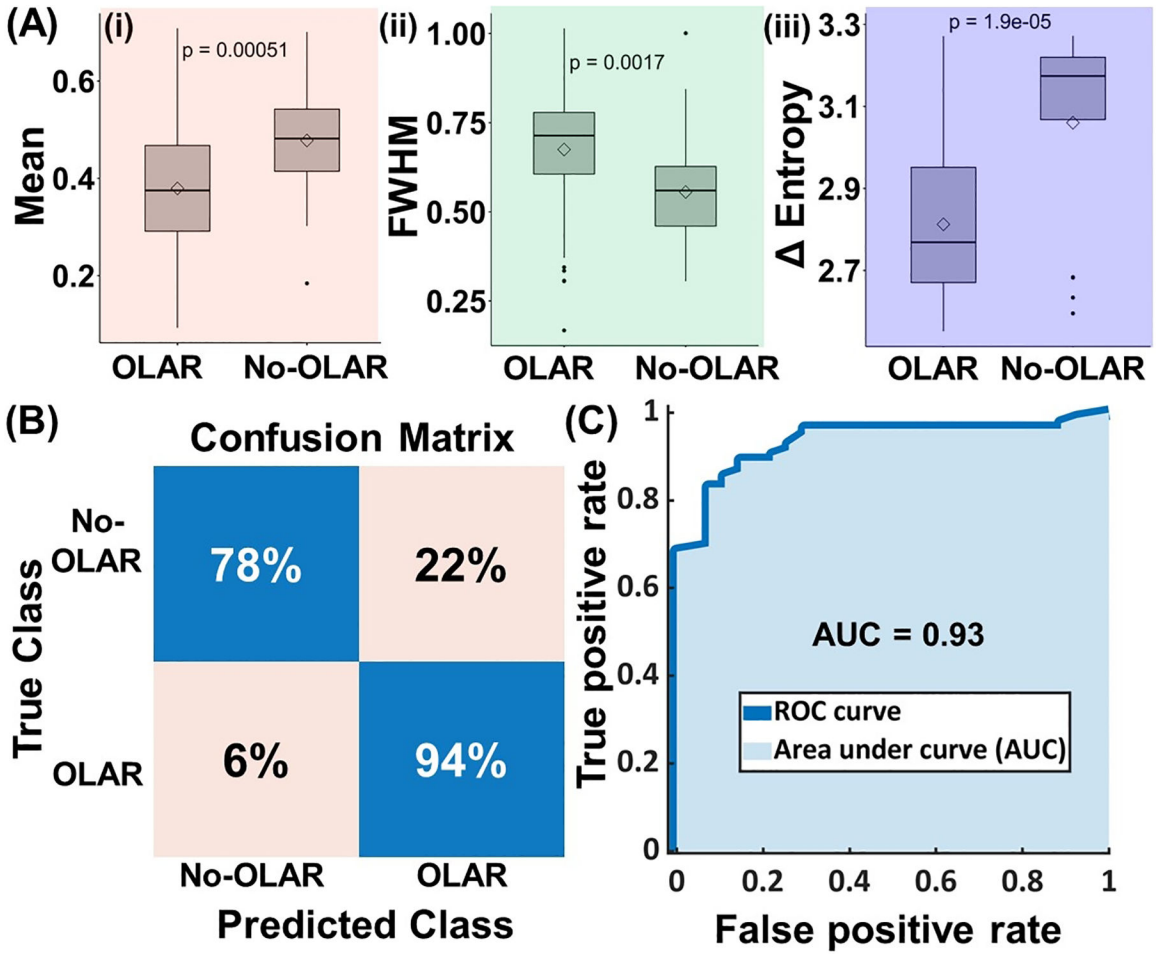


**FIG 4.**

Performance of the classification using three features ensemble classifier, showing (A) a boxplot of (i) SSIM mean, (ii) SSIM FWHM, and (iii) Δ entropy for classifying No-OLAR and OLAR with p-value indicated, (B) the Confusion-matrix for the true and false predictions of No-OLAR versus OLAR, (C) the corresponding area under the curve (AUC) plot for the classification of No-OLAR vs OLAR using the machine learning classifier.

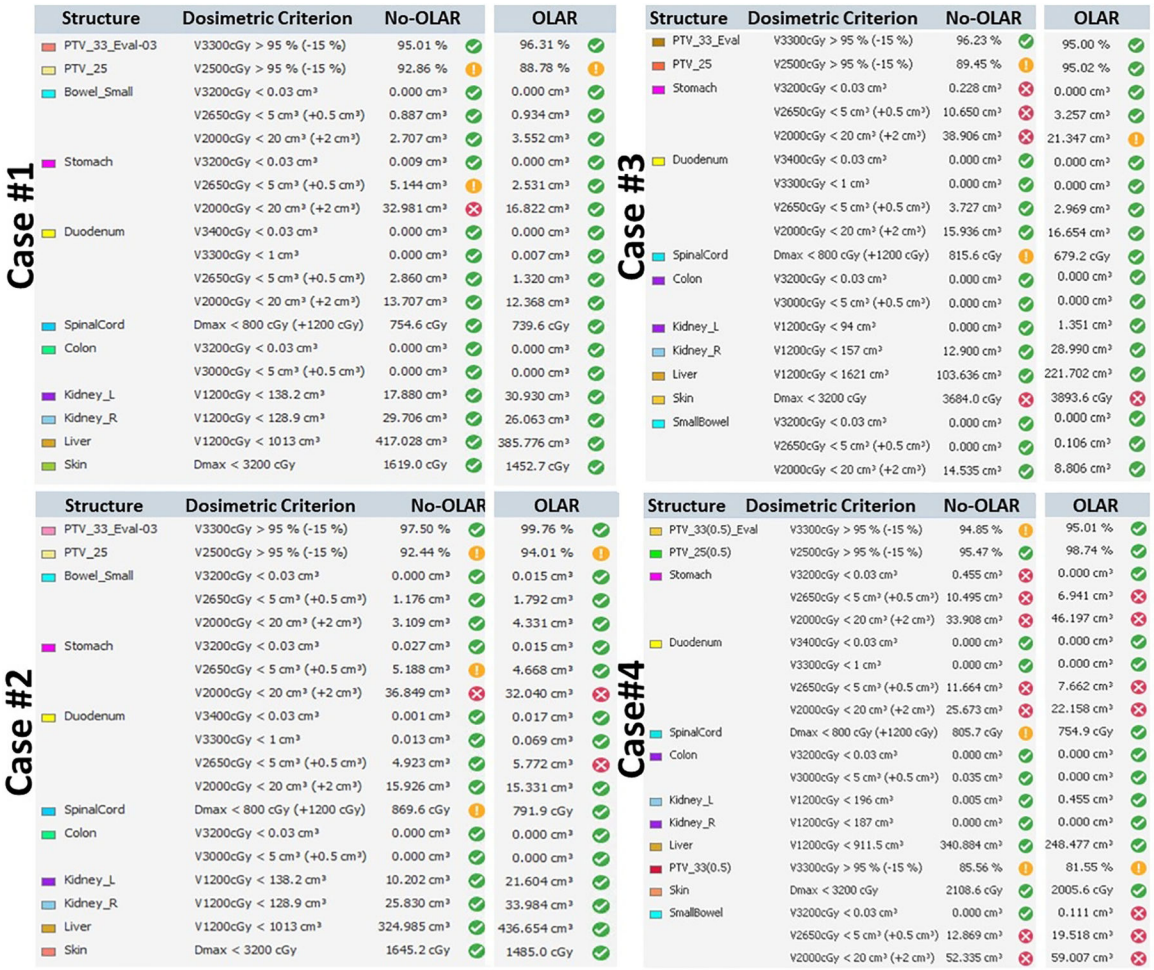


**FIG 5.**

Plan quality comparison of the No-OLAR *vs* OLAR plans for four misclassified fractions (4 cases).

**Table 1.**

Dose volume constraints of PTV and selected OARs for SBRT with a prescription of 3300 cGy in 5 fractions for pancreatic cancer.

| Structure | Dosimetric Criterion | Tolerance |
|---|---|---|
| PTV | $V_{3300cGy} \geq 95\ \%$ | −15% |
| | $V_{2500cGy} \geq 95\ \%$ | −15% |
| Stomach Bowel_Small Colon | $V_{3200cGy} \leq 0.03$ cc | |
| | $V_{2650cGy} \leq 5$ cc | +0.5 cc |
| | $V_{2000cGy} \leq 20$ cc | +2 cc |
| Duodenum | $V_{3400cGy} \leq 0.03$ cc | |
| | $V_{3300cGy} \leq 1$ cc | |
| | $V_{2650cGy} \leq 5$ cc | +0.5 cc |
| | $V_{2000cGy} \leq 20$ cc | +2 cc |
| SpinalCord | $D_{max} \leq 800$ cGy | +1200 cGy |
| Kidney_L | $V_{1200cGy} \leq 75\%$ | |
| Kidney_R | $V_{1200cGy} \leq 75\%$ | |
| Liver | $V_{1200cGy} \leq 50\%$ | |
| Skin | $D_{max} \leq 3200$ cGy | |